Physics and Imaging in Radiation Oncology 26 (2023) 100440

Contents lists available at ScienceDirect

Physics and Imaging in Radiation Oncology

journal homepage: www.sciencedirect.com/journal/physics-and-imaging-in-radiation-oncology

Original Research Article

A deep-learning-based dose verification tool utilizing fluence maps for a cobalt-60 compensator-based intensity-modulated radiation therapy system

Kyuhak Oh [a,b], Mary P. Gronberg [b], Tucker J. Netherton [b,*], Bishwambhar Sengupta [a], Carlos E. Cardenas [c], Laurence E. Court [b], Eric C. Ford [a]

[a] Department of Radiation Oncology, University of Washington Medical Center, Seattle, WA 98195, USA
[b] Department of Radiation Physics, Division of Radiation Oncology, The University of Texas MD Anderson Cancer Center, Houston, TX 77030, USA
[c] Department of Radiation Oncology, University of Alabama, Birmingham, AL 35233, USA

ARTICLE INFO

Keywords:
Deep-learning
Dose prediction
Fluence map
Cobalt-60 compensator-based IMRT

ABSTRACT

Background and purpose: A novel cobalt-60 compensator-based intensity-modulated radiation therapy (IMRT) system was developed for a resource-limited environment but lacked an efficient dose verification algorithm. The aim of this study was to develop a deep-learning-based dose verification algorithm for accurate and rapid dose predictions.

Materials and methods: A deep-learning network was employed to predict the doses from static fields related to beam commissioning. Inputs were a cube-shaped phantom, a beam binary mask, and an intersecting volume of the phantom and beam binary mask, while output was a 3-dimensional (3D) dose. The same network was extended to predict patient-specific doses for head and neck cancers using two different approaches. A field-based method predicted doses for each field and combined all calculated doses into a plan, while the plan-based method combined all nine fluences into a plan to predict doses. Inputs included patient computed tomography (CT) scans, binary beam masks, and fluence maps truncated to the patient's CT in 3D.

Results: For static fields, predictions agreed well with ground truths with average deviations of less than 0.5% for percent depth doses and profiles. Even though the field-based method showed excellent prediction performance for each field, the plan-based method showed better agreement between clinical and predicted dose distributions. The distributed dose deviations for all planned target volumes and organs at risk were within 1.3 Gy. The calculation speed for each case was within two seconds.

Conclusions: A deep-learning-based dose verification tool can accurately and rapidly predict doses for a novel cobalt-60 compensator-based IMRT system.

1. Introduction

A novel compensator-based intensity-modulated radiation therapy (IMRT) system using a cobalt-60 machine has been developed to provide cost-effective and high-quality radiation treatments to low- and middle-income countries (LMICs) [1]. This innovative treatment device utilizes a cobalt-60 source and nine compensators. Each compensator is manufactured by 3-dimensional (3D) printing of a plastic mold, filling on-demand with reusable 2-mm tungsten balls [2]. Currently, the prototype for this system is being manufactured by clinical and engineering collaborators in India. This technology was commissioned into the commercial treatment planning system (TPS) to integrate into the Radiation Planning Assistant (RPA), an automated solution for structure-contouring and treatment-planning in low-resource environments [3,4].

Quality assurance (QA) in radiation therapy ensures the safe implementation of the prescription in terms of the dose to the target volume, minimal dose to normal cells, minimal personal exposure, and adequate patient monitoring [5] and has traditionally focused on verification of the dose delivering the prescribed dose to the patient [6]. There are commercial QA tools for cobalt-60 machines and linac machines [7]. However, in the newly-developed cobalt-60 compensator-based IMRT system, these tools are likely not directly applicable due to the different geometry of the source and compensators. As such, there is no suitable tool to verify the dose calculation in the TPS.

Modern TPSs have used various dose calculation algorithms, including Monte Carlo, pencil beam, convolution/superposition, and

* Corresponding author.
E-mail address: TNetherton@mdanderson.org (T.J. Netherton).

https://doi.org/10.1016/j.phro.2023.100440
Received 13 October 2022; Received in revised form 15 April 2023; Accepted 17 April 2023
Available online 21 April 2023

collapsed cone methods [8-17]; efforts are being made to improve the accuracy and speed of dose calculation using artificial intelligence (AI) technology [18-22]. Various studies of dose prediction have appeared, some of which employ contoured structures as input for various cancer sites such as head and neck [23-25], breast [26], lung [27], prostate [28-30], and rectum [31].

In this study, we have developed a deep-learning-based dose verification method for accurate and efficient dose predictions using our novel compensator-based IMRT system. A neural network is used for 3D dose predictions for static treatment fields and IMRT plans for head and neck cancer (HNC) patients. Our deep-learning engine predicts patient-specific dose distributions using CT scans and fluence maps. Similar studies have been reported [21,32]; however, compared to these studies, converting 2D fluence maps to 3D is simpler and less computationally intensive. The approach should be translatable to other anatomical sites beyond the one for which it was developed and trained.

2. Materials and methods

2.1. Static field dose verification

Dose verification for static fields is an important first step in verifying patient dose as it relates to beam commissioning. Cobalt-60 beam data commissioned into the Eclipse TPS (Varian Medical Systems, Palo Alto, CA, USA) were collected. As shown in Fig. 1(a), inputs comprised a homogeneous binary mask of a cube-shaped water-equivalent phantom, a beam binary mask with higher and lower borders that fit the phantom's height, and an overlapping section of the phantom and beam binary masks while the output is a 3D dose distribution within the phantom. All three input masks are required for the system to function properly; relying solely on the overlapped mask is not sufficient. The water-equivalent phantom data and dose distribution data were exported from Eclipse, and beam binary masks were calculated and generated according to the field size. No density information for the water-equivalent phantom was provided. There were four phantom sizes – $20 \times 20 \times 20$ cm^3, $30 \times 30 \times 30$ cm^3, $40 \times 40 \times 40$ cm^3, and $50 \times 50 \times 50$ cm^3. There were 15 beam fields ranging from 2 ~ 30 cm wide at 2 cm intervals. Source-to-surface distances (SSDs) were affected by both the phantom size and source-to-axis distance (SAD). 80 cm SAD was used, and there were 10 SSDs at 1 cm intervals ranging from SSD-5 cm to SSD + 4 cm. A total of 600 data sets were generated, then randomly divided into 480–60-60 sets for training, validation, and testing. Input and output spatial dimensions were (256,256,256,3) and (256,256,256,1), respectively.

2.2. Patient-specific dose verification

Physician-approved volumetric modulated arc therapy (VMAT) plans for 45 head and neck cancer cases [4] were collected, de-identified according to a protocol approved by the institutional review board of the University of Texas MD Anderson Cancer Center, and then re-planned to create cobalt-60 compensator-based 9 fields IMRT plans using the same initial contours and dose prescriptions from the original VMAT plans. The angles employed in these IMRT plans ranged from 0 to 320 degrees, with intervals of 40 degrees. Then, patient-specific dose prediction was accomplished using two approaches: 1) Each of the 9 fields within the plan was treated as a separate field dose calculation to yield 405 sets. For training, validation, and testing, these were separated into 333-36-36 sets. Patient CT scans, binary beam masks that overlapped with patient CT scans, and fluence maps that overlapped with patient CT scans were employed as inputs, with the patient-specific 3D dose distribution for one field as the output (Fig. 1(b)). Patient CT scans and binary beam masks that overlapped with patient CT scans were normalized from 0 to 1. The fluence map was projected in 3D. The resulting predicted dose distributions for 9 fields corresponding to a single plan were combined to create the total dose for the plan. 2) In addition to the 45 existing plans, we expanded the data set to include an additional 92 IMRT plans created from physician-approved RPA plans. In this case, 9 beam field masks, as well as 9 fluence maps, were combined into one for each plan, resulting in a total of 137 sets that were then divided into 111-13-13 training, validation, and testing sets. The inputs and outputs were identical to those of the previous approach (Fig. 1(c)).

The Eclipse TPS calculated the dose in each voxel of a patient based on the energy-dependent fluence [33]. In contrast to linac, a cobalt-60 beam has a discrete energy spectrum, so fluence is meaningful as a direct input to the dose calculation. The fluence intensity exported from

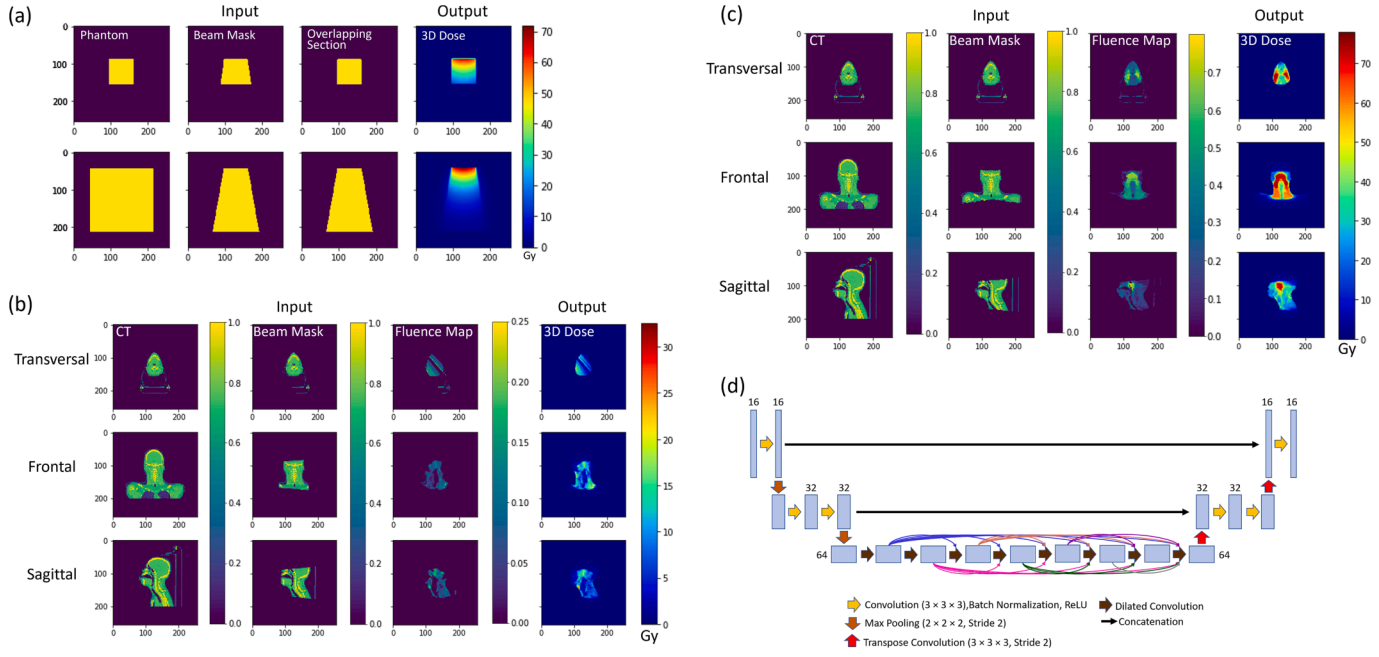

Fig. 1. Input and output data for (a) static field dose verification, (b) field-based patient-specific dose verification, (c) plan-based patient-specific dose verification, and (d) schematic diagram of 3D Dense Dilated U-Net module.

the Eclipse had a range from 0 to 1, and it determined the delivered doses based on the prescribed target doses [34]. Since the format of the fluence map is 2D, it needed to be converted to 3D. A broad beam ray-tracing algorithm and a 3D digital differential analyzer algorithm have been employed to project the fluence maps onto the dose domain in previous studies [21,32]; however, we adopted a simpler method. The 2D fluence map was extended in line with the beam divergence, utilizing the SAD as a reference point. No attenuation was incorporated in order to reduce computational complexity. The spatial dimensions of the input and output were (256,256,256,3) and (256,256,256,1), respectively.

2.3. Deep-learning framework for dose prediction

We investigated multiple deep-learning models for 3D dose prediction in patients with HNC and discovered that the 3D dense dilated U-Net (3D DDU-Net) performed the best [24]. 3D DDU-Net (Fig. 1(d)) is a more advanced version of the fully dense U-Net, which has been shown to outperform the conventional U-Net [35]. Unlike other U-Net architectures, this model employed two encoding paths and two decoding paths, as well as continuous densely-connected dilated convolutions at the bottom stage. Each convolution in the densely-connected stage at the bottom is linked to all subsequent convolutions. The batch normalization is chosen to prevent overfitting during training [36], and ReLU is faster to compute than the sigmoid function, making a considerable difference in neural network training time [37]. The mean squared error (MSE) loss was minimized based on the Adam optimization with an initial learning rate of 1.0E-04, and a batch size of 1 and MSE was employed to quantify the difference between the ground truth dose and the predicted dose for each sample. The epoch was set at 10,000, and the early stopping function was activated to terminate the training if the model performance for validation sets did not improve after a large number of epochs had passed.

2.4. Quantitative analysis

Percent depth doses (PDDs) and in-plane dose profiles were extracted from the dose distribution of the static fields predicted by the deep-learning model. The average percent deviations over multiple phantom sizes, beam field sizes, and SSDs were compared to ground truth data from Eclipse TPS for verification. Furthermore, the ground truth and predicted dose distributions for each static field were used to evaluate gamma passing rates.

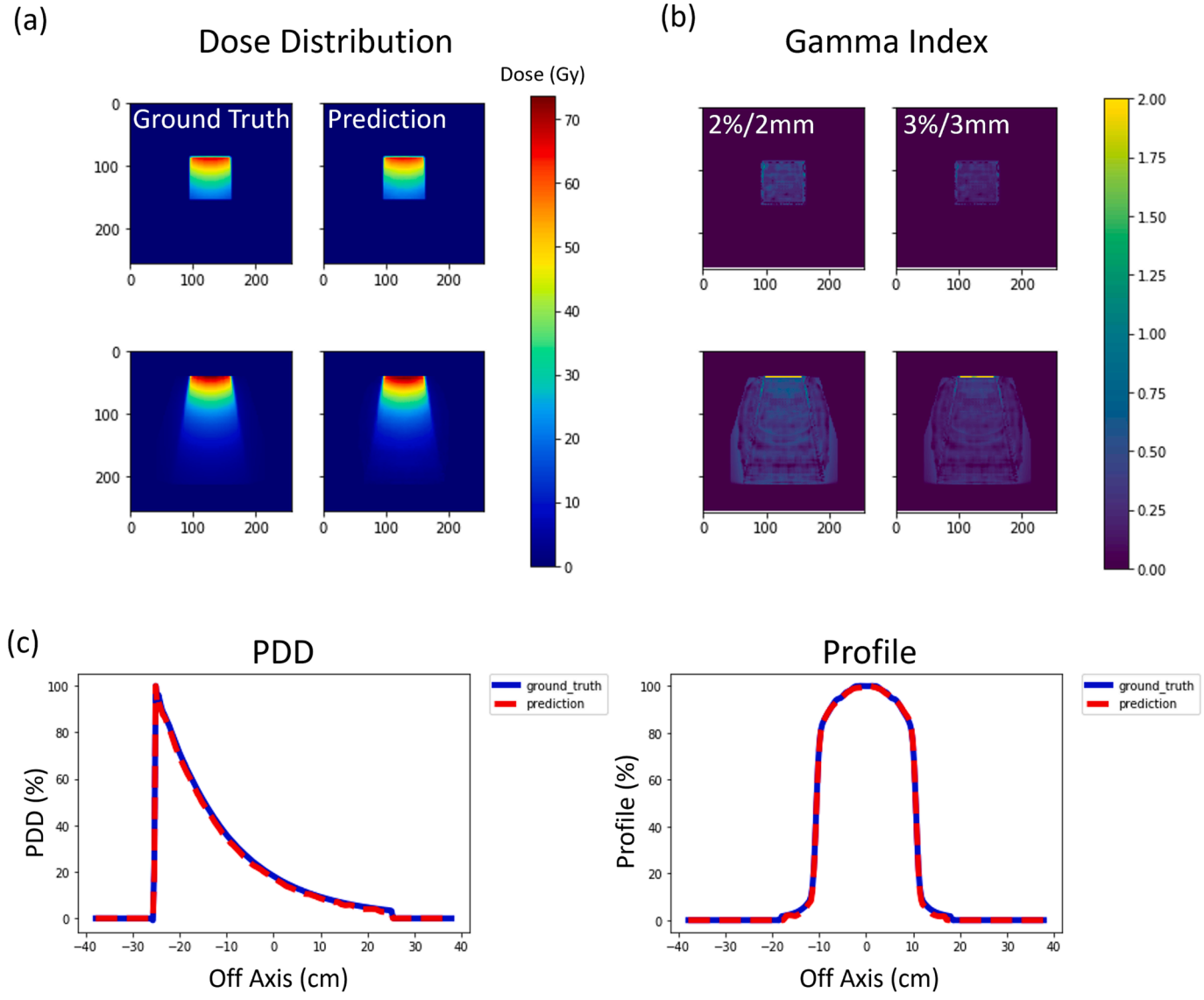

Fig. 2. (a) Dose distributions at the isocenter for ground truth and prediction, (b) corresponding gamma indices with criteria of 2%/2 mm and 3%/3 mm, and (c) PDD and profile comparisons for ground truth and predicted dose based on a representative case in the test set.

Predicted doses were compared to clinical doses based on a compensator-based IMRT system commissioned in Eclipse for patient-specific dose verification [38]. Gamma analysis was performed on the transversal plane at the isocenter to compare the predicted doses to the clinical doses for each plan. The deep-learning-based dose verification system was tested by comparing dose-volume histograms (DVHs) of clinical and predicted dose distributions, followed by statistical assessments for PTVs and OARs. Since the sample size (N = 13) is smaller than 15, the median and range were used for the statistical analysis. For PTVs, $D_{98\%}$, $D_{95\%}$, $D_{5\%}$, D_{max}, D_{min}, and D_{mean} were evaluated. D_{max} was evaluated for the spinal cord, optic nerve, lens, eyes, cochleae, chiasm, brain stem, and brain, whereas D_{mean} was evaluated for parotid glands.

3. Results

As shown in Fig. 2(a) and (b), the predicted doses of the static fields by the deep-learning-based dose prediction tool had an excellent agreement with the ground truths having 99.9 % and 100.0 % average gamma passing rates for 2 mm/3% and 3 mm/3% criteria. In a representative case, Fig. 2(c) showed a good agreement between the PDDs and profiles from the ground truth and prediction. All PDDs and profiles had average percent deviations of 0.4 ± 0.4% and 0.3 ± 0.5%, respectively, across different phantom sizes, SSDs, and field sizes.

Fig. 3 showed the DVHs for each field from a representative HNC patient, along with the predicted doses by the deep-learning model. The deep-learning model accurately predicted field-based doses. The average gamma passing rate for the criteria of 2 mm/2% was nearly 100.0%, and the mean absolute errors were in the range from 0.2 to 0.3 Gy. Though this agreement was excellent, small differences were noted. When the predicted doses from all nine fields were summed to provide a predicted plan dose, these small errors in each field accumulated, and the agreement was reduced. Relatively large structures, such as PTVs, were less affected, whereas smaller structures and structures near or outside of the high-dose regions, such as eyes and lenses, were significantly affected.

Plan-based dose prediction demonstrated better agreement. Fig. 4 illustrates the dose distributions and DVHs between the clinical plan and prediction using a deep-learning model for a representative HNC patient from the test sets. It showed that both doses from the clinical plan and the prediction by the deep-learning model had appropriate coverage for the PTVs and sparing for the OARs. The dose coverage for the PTVs was very similar, with $D_{98\%}$, $D_{95\%}$, $D_{5\%}$, D_{min}, and D_{mean} values within 1%, except for D_{max} (Table 1). Table 2 shows dose differences between clinical and predicted doses for field-based dose prediction and plan-based dose prediction using OAR metrics. The dose distribution by the plan-based dose prediction was much improved over that by field-based dose prediction. Across all OAR metrics, the dose differences between the predicted and clinical doses were less than 1.0 Gy, except for the spinal cord, brain stem and brain.

Moreover, once the model was trained, it took less than two seconds for this deep-learning-based model to predict the 3D dose using a 32 GB GPU node.

4. Discussion

This study assessed a deep-learning-based secondary dose verification system for dose calculation accuracy in both homogeneous and inhomogeneous materials. The gamma analysis and the evaluation for distributed doses were performed for application to static fields associated with the commissioned cobalt-60 beams. As part of the patient-specific dose verification, we evaluated the gamma indices and analyzed the DVHs for PTVs and OARs using compensator-based IMRT plans for HNC patients. The dose was predicted accurately for each case, and the calculation time of this system was less than two seconds. This secondary dose verification system could potentially be used with a compensator-based IMRT system.

Previous studies have used contoured structures combined with patient CT images to predict 3D dose distributions [23,24,26,28,39]. In

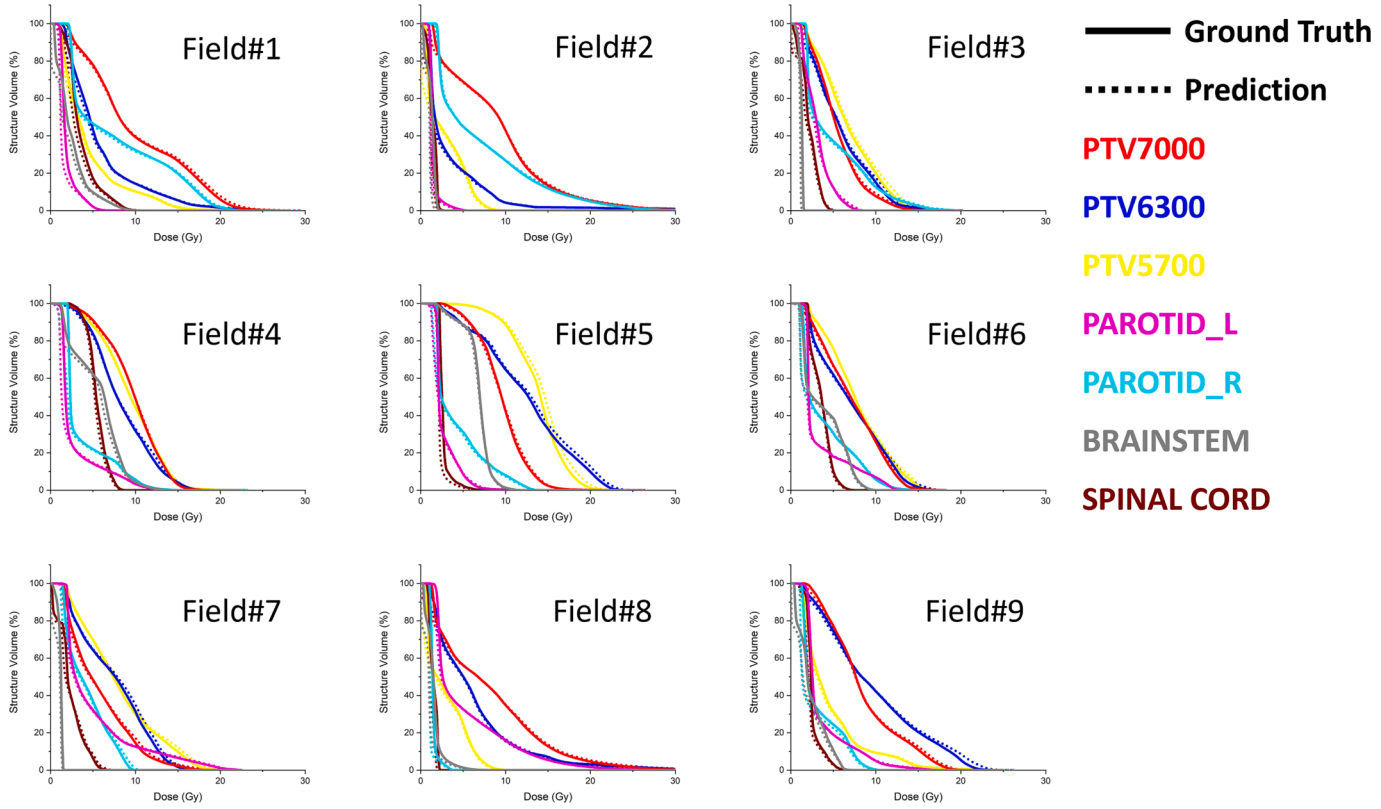

Fig. 3. Field-based DVH analysis for a representative head and neck cancer patient.

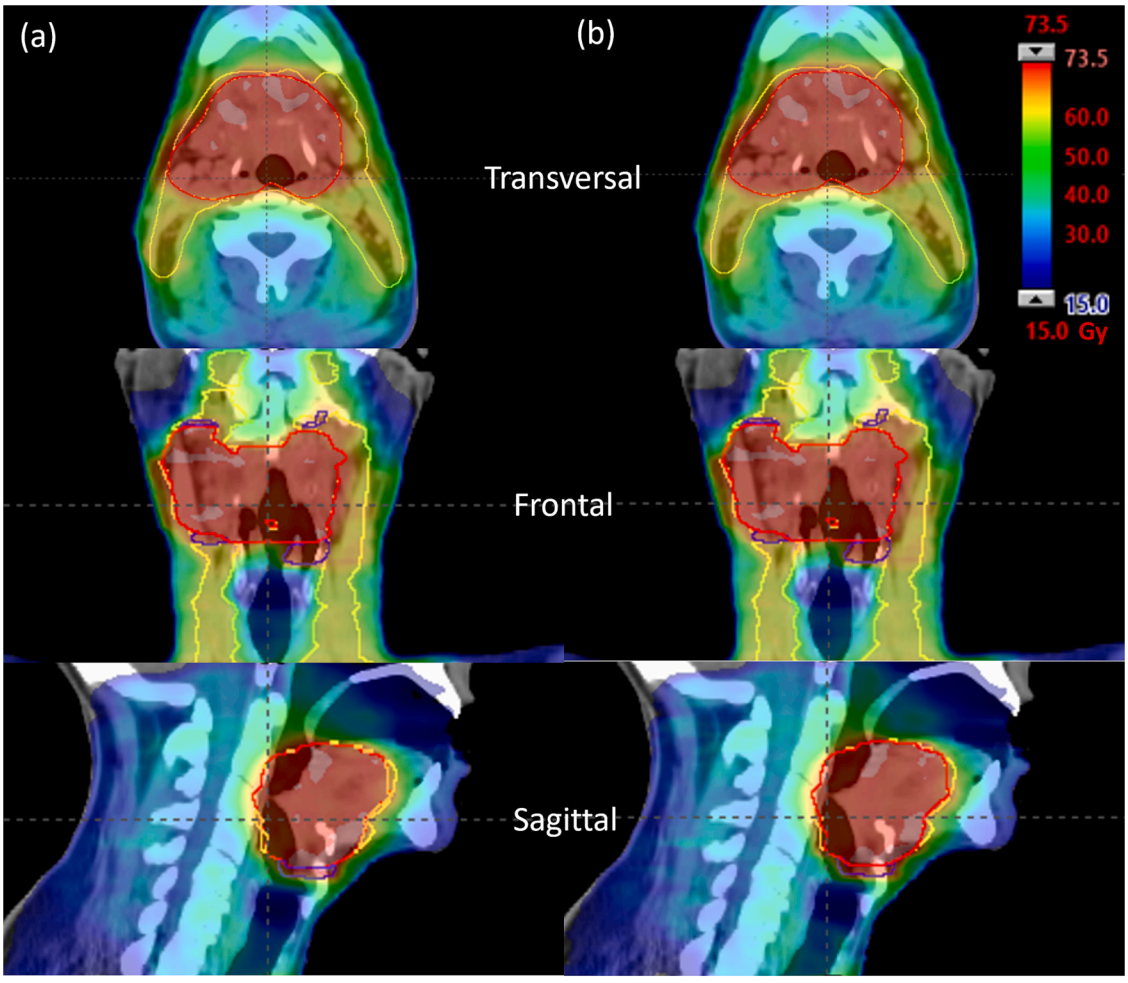

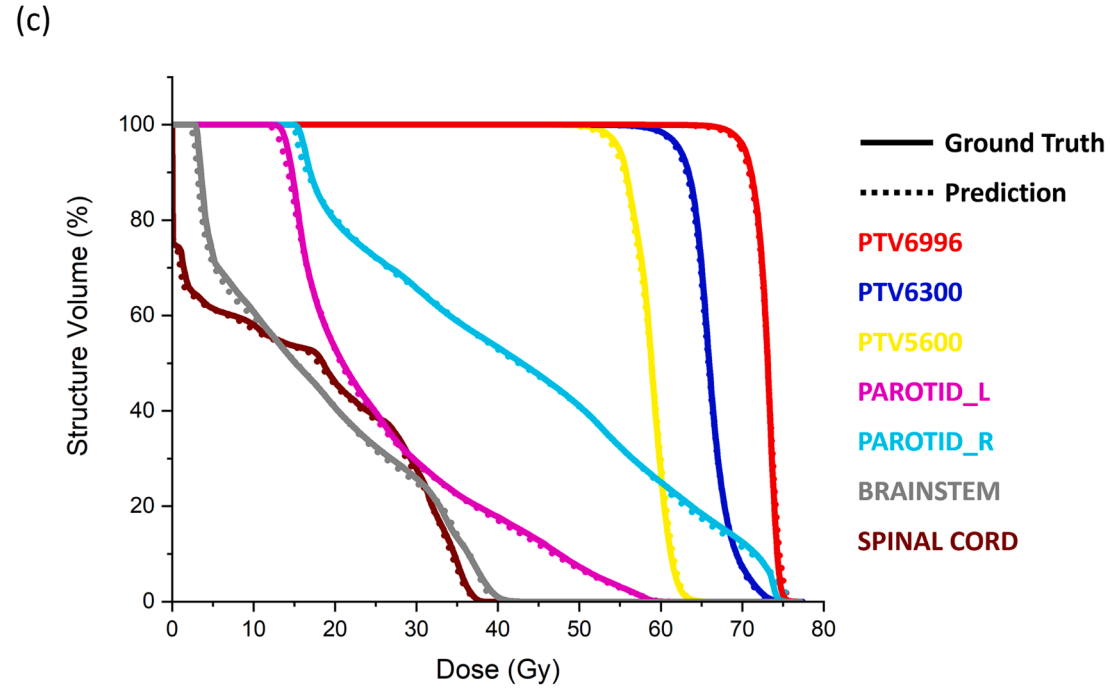

Fig. 4. 3D dose distributions by (a) clinical plan and (b) prediction using the deep-learning model and (c) corresponding dose-volume histograms for the clinical plan (solid lines) and the deep-learning dose prediction (dotted lines) for a representative HNC case.

Table 1
Dose difference (median and range) and percent error between the clinical plan and prediction of the test sets for planning target volumes when using the plan-based dose prediction method (N = 13).

Target	Parameter	Dose Difference (Gy)	Percent Error (%)
PTV1	$D_{98\%}$	0.6(0.3 ~ 1.3)	1.0 ± 0.5
	$D_{95\%}$	0.5(0.2 ~ 0.8)	0.7 ± 0.3
	$D_{5\%}$	−0.4(−0.6 ~ −0.2)	−0.6 ± 0.2
	D_{max}	0.8(−0.1 ~ 3.5)	2.1 ± 2.2
	D_{min}	−0.9(−1.7 ~ 1.0)	−0.8 ± 1.1
	D_{mean}	0.0(0.0 ~ 0.0)	0.0 ± 0.0
PTV2	$D_{98\%}$	0.3(−0.1 ~ 1.3)	0.7 ± 0.7
	$D_{95\%}$	0.3(−0.1 ~ 0.9)	0.5 ± 0.4
	$D_{5\%}$	−0.1(−0.3 ~ 0.3)	−0.1 ± 0.3
	D_{max}	0.6(−3.7 ~ 6.4)	1.6 ± 5.6
	D_{min}	−0.4(−1.0 ~ 1.4)	−0.3 ± 1.0
	D_{mean}	0.0(−0.4 ~ 0.1)	−0.1 ± 0.3
PTV3	$D_{98\%}$	0.4(−1.4 ~ 0.7)	0.3 ± 1.3
	$D_{95\%}$	0.3(−1.3 ~ 0.5)	0.1 ± 1.1
	$D_{5\%}$	0.0(−0.8 ~ 0.2)	−0.1 ± 0.5
	D_{max}	1.1(−0.2 ~ 3.5)	2.8 ± 2.4
	D_{min}	0.2(−1.0 ~ 1.1)	0.0 ± 1.1
	D_{mean}	−0.1(−1.0 ~ 0.2)	−0.3 ± 0.7

Table 2
Dose difference (median and range) comparison between clinical and predicted doses for the field-based dose prediction (N = 4) and the plan-based dose prediction (N = 13) for OAR metrics.

Structure	Constraint	Dose Difference between clinical and predicted doses (Gy)	
		Field-based Dose Prediction	Plan-based Dose Prediction
Spinal Cord	D_{max} < 45 Gy	0.8(0.0 ~ 4.5)	0.5(−1.8 ~ 1.9)
Parotid Gland R	D_{mean} < 26 Gy	2.3(0.7 ~ 3.6)	0.3(0.1 ~ 0.6)
Parotid Gland L	D_{mean} < 26 Gy	2.3(0.0 ~ 10.6)	0.3(0.1 ~ 0.6)
Optic Nerve R	D_{max} < 54 Gy	4.8(4.0 ~ 5.8)	0.6(−0.2 ~ 0.9)
Optic Nerve L	D_{max} < 54 Gy	9.2(6.7 ~ 14.0)	0.6(0.0 ~ 0.9)
Lens_R	D_{max} < 7 Gy	7.9(1.6 ~ 13.1)	0.6(0.3 ~ 0.9)
Lens_L	D_{max} < 7 Gy	8.9(1.7 ~ 12.5)	0.5(0.0 ~ 0.7)
Eye_R	D_{max} < 54 Gy	3.2(1.0 ~ 4.8)	0.5(−0.3 ~ 0.9)
Eye_L	D_{max} < 54 Gy	3.4(1.2 ~ 4.8)	0.5(0.0 ~ 0.8)
Cochlea_R	D_{max} < 35 Gy	6.0(1.7 ~ 12.4)	0.3(−0.4 ~ 0.7)
Cochlea_L	D_{max} < 35 Gy	5.8(2.0 ~ 9.0)	0.3(−0.7 ~ 0.9)
Chiasm	D_{max} < 54 Gy	2.2(1.3 ~ 7.5)	0.6(0.0 ~ 0.9)
Brain Stem	D_{max} < 54 Gy	4.3(0.3 ~ 7.5)	0.3(−0.5 ~ 1.7)
Brain	D_{max} < 60 Gy	7.4(1.6 ~ 11.1)	0.4(−1.3 ~ 1.8)

this work, we used Inputs such as inhomogeneous patient computed tomography (CT) scans, binary beam masks, and fluence maps truncated to the patient CT in 3D. CT scans had inhomogeneous information, which affected the dose distribution, and beam masks provided the boundary lines for the dose distributions. The fluence data has a very close relationship to the dose calculation. A few studies have been conducted using fluence maps with the patient CT scans [21,32], and they used a ray-tracing algorithm to transfer 2D fluence maps to 3D volume data [40,41]. In this study, we used a simpler method to convert a 2D fluence map into 3D data than those studies and confirmed that the dose was accurately predicted using this method.

Another important factor in predicting accurate dose distribution is selecting the appropriate deep-learning model. The majority of studies have used ResNet [32,42], U-Net [18,26,28,39,43], or models derived from U-Net to predict the 3D dose, such as hierarchically densely connected U-Net [21,44]. Nguyen et al. [23] conducted performance tests based on 3D dose predictions on the HNC cases using standard U-Net, dense convolution network, and hierarchically densely connected U-Net (HD U-Net) and showed that the HD U-Net outperformed all other models in terms of dose coverage, dose conformity, and homogeneity. In addition, HD U-Net could predict patient dose more accurately and quickly with fewer parameters than other models. Furthermore, Gronberg et al. [24] evaluated various models, including DeepLabv3+, U-Net, and V-Net, which have traditionally been used for image segmentation, along with the HD U-Net and 3D DDU-Net, which were previously used for dose prediction. As a result of this study, 3D DDU-Net achieved the best performance for patient dose prediction. Although Gronberg et al. [24] used 3D DDU-Net to predict dose based on contoured structures, we used the same deep-learning network for building a fluence-based dose prediction system and achieved good agreement.

It may be possible to extend the prediction model to sites such as prostate, lung, rectum, and breast cancers other than head-and-neck cancer because this deep-learning model predicted the dose for HNC patients with high accuracy, although the treatment plans are relatively complicated. Also, this model may be more flexible than dose prediction models based on contoured structures, where it is necessary to adjust the contoured structures when the cancer site changes. This model simply predicts with the fluence maps, so it is not affected by any changes between cancer sites.

Our results indicate that the deep-learning-based model predicts dose distribution with high accuracy and efficiency. A small error was observed when the field-based dose prediction method was used to predict the 3D dose for each field. However, combining the doses of all 9 fields into one plan resulted in error propagation. A plan-based dose prediction method can resolve this issue because it does not have a combination process, increasing error. There is another model limitation associated with the boundary effect. Like other studies [32,45], the predicted dose in the beam field boundary area appears inconsistent. However, the dose in the beam boundary area is relatively small compared to the dose delivered to the treatment area and lies outside the fluence map boundary; it was determined that boundary effects do not significantly affect the dose prediction. In addition, this research showed that the dose differences were relatively little higher for the spinal cord, brain stem and brain compared to other OARs, although these differences were not statistically significant. This could be attributed to the fact that the volumes of both the spinal cord, brain stem and brain were relatively larger than those of the other OARs.

The deep-learning-based model proposed in this study can be used as a QA tool for secondary dose verification, resulting in significant benefits to cobalt-60 compensator-based IMRT systems in LMICs due to its relatively high efficiency, dose calculation speed, and reliability in predicting doses. Although this study was conducted only focusing on the cobalt-60 compensator-based IMRT system, it should be applicable to other commercially used linac systems that use the IMRT technique, and this will be the subject of further investigations in the future.

Declaration of Competing Interest

The authors declare that they have no known competing financial interests or personal relationships that could have appeared to influence the work reported in this paper.

Acknowledgments

This work was supported by the National Cancer Institute of the National Institutes of Health under Award Number 5UH3 CA211310-04.

References

[1] van Schelt J, Smith DL, Fong N, Toomeh D, Sponseller PA, Brown DW, et al. A ring-based compensator IMRT system optimized for low- and middle-income countries: Design and treatment planning study. Med Phys 2018;45:3275–86. https://doi.org/10.1002/mp.12985.
[2] Toomeh D, Gadoue SM, Fong N, Subrahmanyam G, v., Govindarajan K, Ford EC.. Affordable compensator for IMRT delivery designed for low-and-middle income

countries, a Monte Carlo study. Phys Med 2021;82:211–8. https://doi.org/10.1016/j.ejmp.2021.01.078.
[3] Court LE, Kisling K, McCarroll R, Zhang L, Yang J, Simonds H, et al. Radiation planning assistant – A streamlined, fully automated radiotherapy treatment planning system. J Visu Exp 2018;2018:1–9. https://doi.org/10.3791/57411.
[4] Olanrewaju A, Court LE, Zhang L, Naidoo K, Burger H, Dalvie S, et al. Clinical acceptability of automated radiation treatment planning for head and neck cancer using the radiation planning assistant. Pract Radiat Oncol 2021;11:1–8. https://doi.org/10.1016/j.prro.2020.12.003.
[5] Svensson GK, Baily NA, Loevinger R, Morton RJ, Moyer RF, Purdy JA, et al. Physical aspects of quality assurance in radiation therapy AAPM radiation therapy committee Task Group 24 with contribution by AAPM radiation therapy committee Task Group 22. 1994.
[6] Zhu TC, Stathakis S, Clark JR, Feng W, Georg D, Holmes SM, et al. Report of AAPM Task Group 219 on independent calculation-based dose/MU verification for IMRT. Med Phys 2021;48:e808–29. https://doi.org/10.1002/mp.15069.
[7] Kutcher GJ, Coia L, Gillin M, Hanson WF, Leibei S, Morton RJ, et al. Comprehensive QA for radiation oncology: report of AAPM radiation therapy committee task group 40. Med Phys 1994;21:581–618.
[8] Ahnesjö A. Collapsed cone convolution of radiant energy for photon dose calculation in heterogeneous media. Med Phys 1989;16:577–92. https://doi.org/10.1118/1.596360.
[9] Rogers DWO, Faddegon BA, Ding GX, Ma CM, We J, Mackie TR. BEAM: A Monte Carlo code to simulate radiotherapy treatment units. Med Phys 1995;22:503–24. https://doi.org/10.1118/1.597552.
[10] Liu HH, Mackie TR, McCullough EC. Correcting kernel tilting and hardening in convolution/superposition dose calculations for clinical divergent and polychromatic photon beams. Med Phys 1997;24:1729–41. https://doi.org/10.1118/1.597960.
[11] Bortfeld T, Schlegel W, Rhein B. Decomposition of pencil beam kernels for fast dose calculations in three-dimensional treatment planning. Med Phys 1993;20:311–8. https://doi.org/10.1118/1.597070.
[12] Mackiel TR, Bielajew AF, Rogers DW, Battista JJ. Generation of photon energy deposition kernels using the EGS Monte Carlo code. Phys Med Biol 1988;33:1–20.
[13] Mackie TR, Scrimger JW, Battista JJ. A convolution method of calculating dose for 15 MV X rays. Med Phys 1985;12:188–96. https://doi.org/10.1118/1.595774.
[14] Saxner M, Trepp A. A pencil beam model for photon dose calculation. Med Phys 1992;19:263–73. https://doi.org/10.1118/1.596856.
[15] De Martino F, Clemente S, Graeff C, Palma G, Cella L. Dose calculation algorithms for external radiation therapy: an overview for practitioners. Appl Sci 2021;11:6806. https://doi.org/10.3390/app11156806.
[16] Kim DW, Park K, Kim H, Kim J. History of the Photon Beam Dose Calculation Algorithm in Radiation Treatment Planning System. Prog Med Phys 2020;31:54–62. 10.14316/pmp.2020.31.3.54.
[17] Zhou Z, Song W. A study of dose calculation based on collapsed cone convolution algorithm. 2010 3rd International Conference on Biomedical Engineering and Informatics, Yantai, China, 2010;3:1331–1335. 10.1109/BMEI.2010.5639365.
[18] Kontaxis C, Bol GH, Lagendijk JJW, Raaymakers BW. DeepDose: Towards a fast dose calculation engine for radiation therapy using deep learning. Phys Med Biol 2020:65. https://doi.org/10.1088/1361-6560/ab7630.
[19] Wang Y, Liu Y, Bai Y, Zhou Q, Xu S, Pang X. A generalization performance study on the boosting radiotherapy dose calculation engine based on super-resolution. Med Phys 2023;22:100–3. https://doi.org/10.1016/j.zemedi.2022.10.006.
[20] Wu C, Nguyen D, Xing Y, Montero AB, Schuemann J, Shang H, et al. Improving proton dose calculation accuracy by using deep learning. Mach Learn Sci Technol 2021;2:015017. https://doi.org/10.1088/2632-2153/abb6d5.
[21] Xing Y, Nguyen D, Lu W, Yang M, Jiang S. Technical note: A feasibility study on deep learning-based radiotherapy dose calculation. Med Phys 2020;47:753–8. https://doi.org/10.1002/mp.13953.
[22] Xing Y, Zhang Y, Nguyen D, Lin MH, Lu W, Jiang S. Boosting radiotherapy dose calculation accuracy with deep learning. J Appl Clin Med Phys 2020;21:149–59. https://doi.org/10.1002/acm2.12937.
[23] Nguyen D, Jia X, Sher D, Lin MH, Iqbal Z, Liu H, et al. 3D radiotherapy dose prediction on head and neck cancer patients with a hierarchically densely connected U-net deep learning architecture. Phys Med Biol 2019;64:065020. https://doi.org/10.1088/1361-6560/ab039b.
[24] Gronberg MP, Gay SS, Netherton TJ, Rhee DJ, Court LE, Cardenas CE. Technical note: dose prediction for head and neck radiotherapy using a three-dimensional dense dilated U-net architecture. Med Phys 2021;48:5567–73. https://doi.org/10.1002/mp.14827.
[25] Chen X, Men K, Li Y, Yi J, Dai J. A feasibility study on an automated method to generate patient-specific dose distributions for radiotherapy using deep learning. Med Phys 2019;46:56–64. https://doi.org/10.1002/mp.13262.
[26] Ahn SH, Kim ES, Kim C, Cheon W, Kim M, Lee SB, et al. Deep learning method for prediction of patient-specific dose distribution in breast cancer. Rad Oncol 2021;16:154. https://doi.org/10.1186/s13014-021-01864-9.
[27] Barragán-Montero AM, Nguyen D, Lu W, Lin MH, Norouzi-Kandalan R, Geets X, et al. Three-dimensional dose prediction for lung IMRT patients with deep neural networks: robust learning from heterogeneous beam configurations. Med Phys 2019;46:3679–91. https://doi.org/10.1002/mp.13597.
[28] Ma M, Kovalchuk N, Buyyounouski MK, Xing L, Yang Y. Incorporating dosimetric features into the prediction of 3D VMAT dose distributions using deep convolutional neural network. Phys Med Biol 2019;64:125017. https://doi.org/10.1088/1361-6560/ab2146.
[29] Nguyen D, Long T, Jia X, Lu W, Gu X, Iqbal Z, et al. A feasibility study for predicting optimal radiation therapy dose distributions of prostate cancer patients from patient anatomy using deep learning. Sci Rep 2019;9:1076. https://doi.org/10.1038/s41598-018-37741-x.
[30] Kajikawa T, Kadoya N, Ito K, Takayama Y, Chiba T, Tomori S, et al. A convolutional neural network approach for IMRT dose distribution prediction in prostate cancer patients. J Radiat Res 2019;60:685–93. https://doi.org/10.1093/jrr/rrz051.
[31] Song Y, Hu J, Liu Y, Hu H, Huang Y, Bai S, et al. Dose prediction using a deep neural network for accelerated planning of rectal cancer radiotherapy. Radiot Oncol 2020;149:111–6. https://doi.org/10.1016/j.radonc.2020.05.005.
[32] Fan J, Xing L, Dong P, Wang J, Hu W, Yang Y. Data-driven dose calculation algorithm based on deep U-Net. Phys Med Biol 2020;65:245035. https://doi.org/10.1088/1361-6560/abca05.
[33] Sievinen J, Ulmer W, Kaissl W. AAA Photon Dose Calculation Model in Eclipse™. Palo Alto: 2005.
[34] Varian Medical Systems. Eclipse 11 Commissioning II IMRT, RapidArc. Palo Alto: VMAT; 2014.
[35] Guan S, Hsu K-T, Eyassu M, Chitnis PV. Dense dilated UNet: deep learning for 3D photoacoustic tomography image reconstruction. ArXiv 2021.
[36] Ioffe S, Szegedy C. Batch Normalization: Accelerating Deep Network Training by Reducing Internal Covariate Shift. ArXiv 2015.
[37] Agarap AFM. Deep Learning using Rectified Linear Units (ReLU). ArXiv 2019.
[38] Oh K, Sengupta B, Olanrewaju A, Douglas RJ, Roach KE, Cardenas CE, et al. Commissioning of a novel compensator-based IMRT system for low- and middle-income countries. Med Phys 2021;48.
[39] Mashayekhi M, Tapia IR, Balagopal A, Zhong X, Barkousaraie AS, McBeth R, et al. Site-agnostic 3D dose distribution prediction with deep learning neural networks. Med Phys 2022;49:1391–406. https://doi.org/10.1002/mp.15461.
[40] Woo A, Amanatides J. A fast voxel traversal algorithm for ray tracing. Eurographics 1987;87:3–10.
[41] Lu W, Chen M. Fluence-convolution broad-beam (FCBB) dose calculation. Phys Med Biol 2010;55:7211–29. https://doi.org/10.1088/0031-9155/55/23/003.
[42] Fan J, Wang J, Chen Z, Hu C, Zhang Z, Hu W. Automatic treatment planning based on three-dimensional dose distribution predicted from deep learning technique. Med Phys 2019;46:370–81. https://doi.org/10.1002/mp.13271.
[43] Bakx N, Bluemink H, Hagelaar E, van der Sangen M, Theuws J, Hurkmans C. Development and evaluation of radiotherapy deep learning dose prediction models for breast cancer. Phys Imaging Radiat Oncol 2021;17:65–70. https://doi.org/10.1016/j.phro.2021.01.006.
[44] Lempart M, Benedek H, Nilsson M, Eliasson N, Bäck S, Munck af Rosenschöld P,, et al. Volumetric modulated arc therapy dose prediction and deliverable treatment plan generation for prostate cancer patients using a densely connected deep learning model. Phys Imaging Radiat Oncol 2021;19:112–9. https://doi.org/10.1016/j.phro.2021.07.008.
[45] Jia M, Wu Y, Yang Y, Wang L, Chuang C, Han B, et al. Deep learning-enabled EPID-based 3D dosimetry for dose verification of step-and-shoot radiotherapy. Med Phys 2021;48:6810–9. https://doi.org/10.1002/mp.15218.